Oxygen Reduction Mechanism of Monometallic Rhodium Hydride Complexes

Robert L. Halbach,[†,‡] Thomas S. Teets,[†,§] and Daniel G. Nocera*,[†,‡]

[†]Department of Chemistry, 6-335, Massachusetts Institute of Technology, 77 Massachusetts Avenue, Cambridge, Massachusetts 02139-4307, United States

[‡]Department of Chemistry and Chemical Biology, Harvard University, 12 Oxford Street, Cambridge, Massachusetts 02138-2902, United States

[§]Department of Chemistry, University of Houston, 112 Fleming Building Houston, Texas 77204-5003, United States

Ⓢ Supporting Information

ABSTRACT: The reduction of O_2 to H_2O mediated by a series of electronically varied rhodium hydride complexes of the form $cis,trans$-$Rh^{III}Cl_2H(CNAd)(P(4\text{-}X\text{-}C_6H_4)_3)_2$ (2) (CNAd = 1-adamantylisocyanide; X = F (2a), Cl (2b), Me (2c), OMe (2d)) was examined through synthetic and kinetic studies. Rhodium(III) hydride 2 reacts with O_2 to afford H_2O with concomitant generation of $trans$-$Rh^{III}Cl_3(CNAd)(P(4\text{-}X\text{-}C_6H_4)_3)_2$ (3). Kinetic studies of the reaction of the hydride complex 2 with O_2 in the presence of HCl revealed a two-term rate law consistent with an HX reductive elimination (HXRE) mechanism, where O_2 binds to a rhodium(I) metal center and generates an η^2-peroxo complex intermediate, $trans$-$Rh^{III}Cl(CNAd)(\eta^2\text{-}O_2)(P(4\text{-}X\text{-}C_6H_4)_3)_2$ (4), and a hydrogen-atom abstraction (HAA) mechanism, which entails the direct reaction of O_2 with the hydride. Experimental data reveal that the rate of reduction of O_2 to H_2O is enhanced by electron-withdrawing phosphine ligands. Complex 4 was independently prepared by the addition of O_2 to $trans$-$Rh^ICl(CNAd)(P(4\text{-}X\text{-}C_6H_4)_3)_2$ (1). The reactivity of 4 toward HCl reveals that such peroxo complexes are plausible intermediates in the reduction of O_2 to H_2O. These results show that the given series of electronically varied rhodium(III) hydride complexes facilitate the reduction of O_2 to H_2O according to a two-term rate law comprising HXRE and HAA pathways and that the relative rates of these two pathways, which can occur simultaneously and competitively, can be systematically modulated by variation of the electronic properties of the ancillary ligand set.
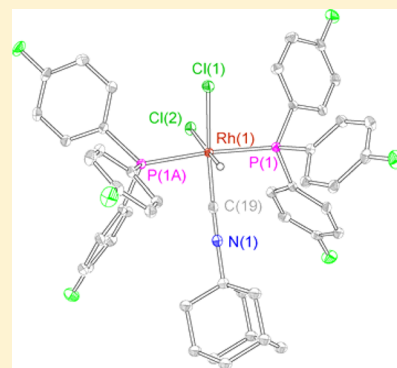
INTRODUCTION

Molecular oxygen is considered to be an ideal oxidant given its availability and low cost. As a result, there is considerable appeal in developing chemical systems that utilize O_2 as the primary oxidizing species.[1−3] In this light, the selective reduction of O_2 mediated by transition metal complexes is of continuing interest on several fronts, as this transformation offers insight into the design of both biomimetic and nonbiomimetic catalysts that use O_2 as the sole oxidizing species.[4−13] Insertion of O_2 into metal hydride bonds is often a key step in its activation, and metal hydroperoxide complexes are frequently the observed products of this reaction. Indeed, such reactions have been observed for hydride complexes of cobalt,[14] iridium,[15] palladium,[16,17] platinum,[18,19] and rhodium.[20−23] Accordingly, studies of the reaction of O_2 with metal hydride complexes are germane to expanding the scope and utility of aerobic oxidation reactions.

Previous work from our group has shown that dirhodium hydride complexes mediate the overall four-electron/four-proton reduction of O_2 to H_2O.[24] Synthetic and kinetic studies of the dirhodium hydride, $Rh_2^{II,II}(tfepma)_2(CN^tBu)_2Cl_3H$ (tfepma = $MeN[P(OCH_2CF_3)_2]_2$, CN^tBu = $tert$-butylisocyanide), as well as the diiridium analogue, established a

mechanistic basis for the oxygen reduction reaction (ORR) of O_2 to H_2O mediated by group 9 bimetallic hydride complexes.[25] Although radical chain autoxidation pathways have been observed for some systems,[18,19,26] the two most commonly observed pathways for the insertion of O_2 into a metal hydride bond are (i) the HX reductive elimination (HXRE) pathway,[23,27−29] which entails HX reductive elimination from the metal complex, binding of O_2 to the reduced metal center, and protonation of the bound peroxo; and (ii) the H atom abstraction (HAA) pathway,[17,30−32] in which O_2 reacts directly with the metal hydride. In some systems, these two pathways are computationally and experimentally found to be kinetically competitive and can even occur simultaneously.[25,30,33,34]

In order to probe the nature of the competition between the HXRE and HAA pathways, we sought to investigate the electronic factors that dictate the relative importance of these two mechanisms in ORRs mediated by rhodium hydride complexes. Two-electron mixed valent dirhodium hydride systems perform the ORR, but a systematic kinetics evaluation

is difficult because there are few synthetic handles to enable the electronic properties of the metal complex to be varied. Additionally, we have demonstrated that the monometallic rhodium hydride complex of the form cis,trans-Rh^{III}Cl$_2$H(L)-(PEt$_3$)$_2$ (where L = CO, 2,6-dimethylphenylisocyanide or 1-adamantylisocyanide (CNAd)) performs the ORR.[35] However, these monometallic rhodium hydride complexes perform the ORR on a time scale that is prohibitively slow for in-depth mechanistic studies.

In order to uncover the mechanism(s) of the ORR facilitated by the aforementioned rhodium hydride complexes, a new ancillary ligand set was sought for the monometallic rhodium system that would accelerate ORR kinetics. Substitution of the PEt$_3$ ligands for PPh$_3$ ligands greatly enhances the rate of the ORR such that the reduction of O$_2$ to water in the presence of HCl occurs on the time scale of minutes as opposed to several days. In addition, facile variation of the substituent at the para position of the aryl rings of the triaryl phosphine ligands P(4-X-C$_6$H$_4$)$_3$ (where X = F, Cl, Me, OMe) permits tuning of the electronic properties of the rhodium metal center, allowing for the evaluation of the impact of ancillary ligand electronic properties on the course of the ORR.

We report here a mechanistic study of the ORR for electronically variegated monometallic rhodium hydride complexes of the form cis,trans-Rh^{III}Cl$_2$H(CNAd)(P(4-X-C$_6$H$_4$)$_3$)$_2$ (**2**) (where X = F (**2a**), Cl (**2b**), Me (**2c**), OMe (**2d**)) in order to determine what factors, particularly with regard to ligand environment, govern the kinetics and preferred mechanistic pathways of aerobic oxidation reactions for metal hydride complexes. We demonstrate that systematic variation of the electronic properties of the monometallic rhodium hydride complexes leads to systematic variation in the rates of the HXRE and HAA pathways. Treatment of trans-Rh^{I}Cl(CNAd)-(P(4-X-C$_6$H$_4$)$_3$)$_2$ (**1**) species with O$_2$ furnishes trans-Rh^{III}Cl-(CNAd)(η^2-O$_2$)(P(4-X-C$_6$H$_4$)$_3$)$_2$ (**4**), which establishes a peroxo complex as a key intermediate in the ORR chemistry of the monometallic rhodium hydrides.

■ EXPERIMENTAL SECTION

General Considerations. All manipulations and reactions, with the exception of oxygenation reactions, were carried out under dry N$_2$ using standard Schlenk and glovebox techniques. Solvents were dried by passage through an alumina column under argon and stored over 4 Å molecular sieves for at least 12 h prior to use. Benzene-d$_6$ (C$_6$D$_6$) was distilled from sodium metal, dichloromethane-d$_2$ (CD$_2$Cl$_2$) was distilled from sodium hydride, and THF-d$_8$ was distilled from sodium metal and benzophenone. The deuterated solvents were then stored over 4 Å molecular sieves for at least 12 h prior to use. HCl (4 M in 1,4-dioxane), 2,6-bis(1,1-dimethylethyl)-4-methylphenol (BHT), 1-adamantylisocyanide (CNAd), tris(4-chlorophenyl)phosphine, tris(4-fluorophenyl)phosphine, tris(4-methoxyphenyl)phosphine, and tris(4-tolylphenyl)phosphine were obtained from Sigma-Aldrich, [RhCl-(COD)]$_2$ was obtained from Strem Chemicals, and O$_2$ was obtained from Airgas. All reagents were used as received. Elemental analyses were performed by Midwest Microlab LLC.

Physical Methods. NMR spectra were recorded at the MIT Department of Chemistry Instrumentation Facility on a Varian Mercury 300 NMR Spectrometer or a Varian Inova-500 NMR Spectrometer. ^{31}P{^{1}H} NMR spectra were referenced to an external standard of 85% D$_3$PO$_4$, and ^{1}H NMR spectra were referenced to the residual proteo solvent resonances. UV−vis spectra were recorded at 293 K in THF solutions in quartz cuvettes on a Varian Cary 5000 UV−vis-NIR spectrophotometer. Extinction coefficients were determined over a concentration range between 10^{-6} and 10^{-4} M, for which all compounds obeyed Beer's Law. UV−vis spectra for the hydride

complexes **2** were collected in the presence of 53 mM HCl. UV−vis spectra for the peroxo species **4** were collected in the presence of 1 atm of O$_2$. IR spectra were recorded on a PerkinElmer Spectrum 400 FT-IR/FT-FIR Spectrometer outfitted with a Pike Technologies GladiATR attenuated total reflectance accessory with a monolithic diamond crystal stage and pressure clamp. Samples were suspended in Nujol for all IR measurements.

Kinetic Measurements. All kinetic experiments were monitored by UV−vis spectroscopy. For each of the four different hydride complexes **2a−d**, a 6.46 × 10^{-3} M CH$_2$Cl$_2$ stock solution was prepared in an N$_2$-filled glovebox. The hydride species **2** was generated in situ by the addition of five molar equivalents of HCl using 4.2 M HCl in 1,4-dioxane. ^{31}P{^{1}H} NMR revealed that **2** formed rapidly and quantitatively. Each UV−vis sample was prepared as follows: (1) In the glovebox, 3.50 mL of THF and an appropriate amount of 4.2 M HCl in 1,4-dioxane were added to a quartz cuvette sealed with a septum cap; (2) approximately 500 μL of the stock CH$_2$Cl$_2$ solution of **2** were added to a small vial sealed with a septum cap; (3) on the benchtop, a measured amount of O$_2$ was injected into the quartz cuvette using a gastight syringe, and the cuvette was vigorously shaken to ensure complete mixing and equilibration of O$_2$. Just prior to each kinetics experiment, a 20.0 μL aliquot of the 6.46 × 10^{-3} M stock CH$_2$Cl$_2$ solution of **2** was injected via a micro syringe into the quartz cuvette containing 3.50 mL of THF, a measured excess of HCl in 1,4-dioxane, and a measured excess of O$_2$. Thus, for each sample, the concentration of **2** in THF was 3.69 × 10^{-5} M. As a result, the concentrations of O$_2$ and HCl in the sample are in excess relative to **2**. Immediately following injection of the stock CH$_2$Cl$_2$ solution of **2**, the cuvette was vigorously shaken for a few seconds and then placed in a temperature-controlled cuvette holder. The progress of the reaction was monitored at 293 K by collecting single wavelength absorption data every 0.033 s over five half-lives. Data fitting and analysis were performed using the software OriginPro 8.6.

Preparation of trans-Rh^{I}Cl(CNAd)(P(4-X-C$_6$H$_4$)$_3$)$_2$ (1) (X = F (1a), Cl (1b), Me (1c), OMe (1d)). [RhCl(COD)]$_2$ (100 mg, 0.203 mmol) and a magnetic stirbar were added to a 20 mL scintillation vial. Approximately 2 mL of THF was added to the vial to give an orange suspension. A solution of P(4−F-C$_6$H$_4$)$_3$ (257 mg, 0.813 mmol, 4.00 equiv) in 2 mL of THF was then added to the vial, followed by a solution of CNAd (65.4 mg, 0.406 mmol, 2.00 equiv) in 2 mL of THF. The resultant mixture was stirred at 20 °C for 1 h, during which time the orange suspension became a yellow solution. Then, the solution was taken to dryness in vacuo to give a yellow solid, which was triturated with 10 mL of pentane. The pentane was decanted, and the remaining fine yellow powder was dried in vacuo at 20 °C to remove residual solvent. Yield: 360 mg (95%). ^{1}H NMR (500 MHz, C$_6$D$_6$) δ/ppm: 0.97 (br, d, 6H), 1.13 (br, m, 6H), 1.51 (br, m, 3H), 6.79 (m, 12H), 7.79 (m, 12H). ^{31}P{^{1}H} NMR (121.5 MHz, C$_6$D$_6$) δ/ppm: 30.9 (d, $^1J_{Rh−P}$ = 140 Hz). UV−vis (THF): λ/nm (ε/M^{-1} cm^{-1}) 248 (32 100), 302 (14 000), 371 (3910). IR (Nujol): $\tilde{\nu}_{C≡N}$ = 2111 cm^{-1}. Anal. Calcd for C$_{47}$ClF$_6$H$_{39}$NP$_2$Rh: C, 60.56; H, 4.22; N, 1.50. Found: C, 60.53; H, 4.31; N, 1.48.

Complex **1b**: 89% yield; ^{1}H NMR (500 MHz, C$_6$D$_6$) δ/ppm: 0.94 (br, d, 6H), 1.20 (br, m, 6H), 1.57 (br, m, 3H), 7.09 (d, 12H), 7.69 (m, 12H). ^{31}P{^{1}H} NMR (121.5 MHz, C$_6$D$_6$) δ/ppm: 31.4 (d, $^1J_{Rh−P}$ = 140 Hz). UV−vis (THF): λ/nm (ε/M^{-1} cm^{-1}) 233 (72 400), 260(sh) (30 800), 306 (14 200), 381 (3345). IR (Nujol): $\tilde{\nu}_{C≡N}$ = 2101 cm^{-1}. Anal. Calcd for C$_{47}$Cl$_7$H$_{39}$NP$_2$Rh: C, 54.76; H, 3.81; N, 1.36. Found: C, 54.69; H, 3.95; N, 1.40.

Complex **1c**: 99% yield; ^{1}H NMR (500 MHz, C$_6$D$_6$) δ/ppm: 1.04 (br, d, 6H), 1.18 (br, m, 6H), 1.42 (br, m, 3H), 2.03 (s, 18H), 6.99 (d, 12H), 8.11 (m, 12H). ^{31}P{^{1}H} NMR (121.5 MHz, C$_6$D$_6$) δ/ppm: 30.9 (d, $^1J_{Rh−P}$ = 137 Hz). UV−vis (THF): λ/nm (ε/M^{-1} cm^{-1}) 235(sh) (56 800), 255 (sh) (36 200), 305 (15 200), 378 (3960). IR (Nujol): $\tilde{\nu}_{C≡N}$ = 2085 cm^{-1}. Anal. Calcd for C$_{53}$ClH$_{57}$NP$_2$Rh: C, 70.08; H, 6.32; N, 1.54. Found: C, 70.12; H, 6.46; N, 1.64.

Complex **1d**: 99% yield; ^{1}H NMR (500 MHz, C$_6$D$_6$) δ/ppm: 1.14 (br, d, 6H), 1.20 (br, m, 6H), 1.56 (br, m, 3H), 3.24 (s, 18H), 6.80 (d, 12H), 8.13 (m, 12H). ^{31}P{^{1}H} NMR (121.5 MHz, C$_6$D$_6$) δ/ppm: 28.7 (d, $^1J_{Rh−P}$ = 136 Hz). UV−vis (THF): λ/nm (ε/M^{-1} cm^{-1}) 243 (77

900), 264(sh) (43 800), 304 (17 000), 375 (4140). IR (Nujol): $\tilde{\nu}_{C\equiv N}$ = 2072 cm^{-1}. Anal. Calcd for $C_{53}ClH_{57}NO_6P_2Rh$: C, 63.38; H, 5.72; N, 1.39. Found: C, 63.12; H, 5.94; N, 1.36.

Preparation of cis,trans-Rh^{III}Cl$_2$H(CNAd)(P(4-X-C$_6$H$_4$)$_3$)$_2$ (2) (X = F (2a), Cl (2b), Me (2c), OMe (2d)). Complex **1a** (100 mg, 0.107 mmol) and a magnetic stirbar were added to a 20 mL scintillation vial. The solid was dissolved in 2 mL of CH_2Cl_2 to give a clear, yellow solution. A solution of HCl in 1,4-dioxane (4.2 M, 0.25 mL, 10 equiv) was added to the vial, and the mixture immediately became a clear faintly yellow solution. The solution was then stirred at 20 °C for 1 h before being taken to dryness in vacuo. The resultant off-white solid was suspended in roughly 10 mL of pentane, and a few drops of a solution of HCl in 1,4-dioxane were added to the suspension. The mixture was stirred, and the solid became white. The contents of the vial were allowed to settle, and the pentane was removed by pipet. The resultant fine white solid was dried in vacuo at 20 °C to remove residual solvent. Yield: 103 mg (99%). ^{1}H NMR (500 MHz, CD$_2$Cl$_2$) δ/ppm: −14.75 (dt, 1H, $^1J_{Rh-H}$ = 15.0 Hz, $^2J_{P-H}$ = 12.5 Hz), 1.13 (br, d, 6H), 1.42 (br, m, 6H), 1.85 (br, m, 3H), 7.14 (m, 12H), 7.89 (m, 12H). ^{31}P{^{1}H} NMR (121.5 MHz, CD$_2$Cl$_2$) δ/ppm: 24.3 (d, $^1J_{Rh-P}$ = 94 Hz). UV−vis (THF): λ/nm (ε/M^{-1} cm^{-1}) 262(sh) (19 400), 268 (20 000), 274(sh) (18 600), 280(sh) (15 600), 308 (14 000). IR (Nujol): $\tilde{\nu}_{Rh-H}$ = 2124 cm^{-1}. Anal. Calcd for $C_{47}Cl_2F_6H_{40}NP_2Rh$: C, 58.28; H, 4.16; N, 1.45. Found: C, 57.81; H, 4.15; N, 1.50. Crystals suitable for single-crystal diffraction analysis were obtained from a CH_2Cl_2 solution of **2** in the presence of excess HCl layered with pentane.

Complex 2b. 94% yield; ^{1}H NMR (500 MHz, CD$_2$Cl$_2$) δ/ppm: −14.44 (dt, 1H, $^1J_{Rh-H}$ = 15.0 Hz, $^2J_{P-H}$ = 12.5 Hz), 1.09 (br, d, 6H), 1.45 (br, m, 6H), 1.86 (br, m, 3H), 7.42 (m, 12H), 7.74 (m, 12H). ^{31}P{^{1}H} NMR (121.5 MHz, CD$_2$Cl$_2$) δ/ppm: 25.4 (d, $^1J_{Rh-P}$ = 94 Hz). UV−vis (THF): λ/nm (ε/M^{-1} cm^{-1}) 273(sh) (23 600), 280(sh) (23 000), 314 (15 800). IR (Nujol): $\tilde{\nu}_{Rh-H}$ = 2102 cm^{-1}. Anal. Calcd for $C_{47}Cl_8H_{40}NP_2Rh$: C, 52.89; H, 3.78; N, 1.31. Found: C, 52.66; H, 3.75; N, 1.31.

Complex 2c. 96% yield; ^{1}H NMR (500 MHz, CD$_2$Cl$_2$) δ/ppm: −14.65 (dt, 1H, $^1J_{Rh-H}$ = 15.0 Hz, $^2J_{P-H}$ = 12.5 Hz), 1.04 (br, d, 6H), 1.38 (br, m, 6H), 1.79 (br, m, 3H), 2.36 (s, 18H), 7.20 (d, 12H), 7.67 (m, 12H). ^{31}P{^{1}H} NMR (121.5 MHz, CD$_2$Cl$_2$) δ/ppm: 23.9 (d, $^1J_{Rh-P}$ = 92 Hz). UV−vis (THF): λ/nm (ε/M^{-1} cm^{-1}) 270 (16 400), 278 (15 600), 314 (14 700). IR (Nujol): $\tilde{\nu}_{Rh-H}$ = 2082 cm^{-1}. Anal. Calcd for $C_{53}Cl_2H_{58}NP_2Rh$: C, 67.38; H, 6.19; N, 1.48. Found: C, 67.28; H, 6.24; N, 1.46.

Complex 2d. 99% yield; ^{1}H NMR (500 MHz, CD$_2$Cl$_2$) δ/ppm: −14.71 (dt, 1H, $^1J_{Rh-H}$ = 15.0 Hz, $^2J_{P-H}$ = 12.5 Hz), 1.11 (br, d, 6H), 1.39 (br, m, 6H), 1.80 (br, m, 3H), 3.82 (s, 18H), 6.92 (m, 12H), 7.70 (m, 12H). ^{31}P{^{1}H} NMR (121.5 MHz, CD$_2$Cl$_2$) δ/ppm: 21.9 (d, $^1J_{Rh-P}$ = 91 Hz). UV−vis (THF): λ/nm (ε/M^{-1} cm^{-1}) 249 (59 700), 277 (28 500), 285 (23 100), 317 (19 800). IR (Nujol): $\tilde{\nu}_{Rh-H}$ = 2120 cm^{-1}. Anal. Calcd for $C_{53}Cl_2H_{58}NO_6P_2Rh$: C, 61.16; H, 5.62; N, 1.35. Found: C, 61.09; H, 5.56; N, 1.34.

Preparation of trans-Rh^{III}Cl$_3$(CNAd)(P(4-X-C$_6$H$_4$)$_3$)$_2$ (3) (X = F (3a), Cl (3b), Me (3c), OMe (3d)). Complex **1a** (100 mg, 0.107 mmol) was added to a scintillation vial along with a magnetic stirbar. The solid was dissolved in 2 mL of CH_2Cl_2 to give a clear yellow solution. A solution of PhICl$_2$ (29.4 mg, 0.107 mmol, 1.00 equiv) was added to the vial to give a yellow-orange solution. The contents of the vial were stirred at 20 °C for 30 min before being taken to dryness in vacuo. The resultant yellow-orange solid was washed with 3 × 10 mL portions of pentane and then pumped in vacuo at 20 °C overnight to give a fine yellow-orange solid. Yield: 105 mg (97%). ^{1}H NMR (500 MHz, C$_6$D$_6$) δ/ppm: 1.12 (br, d, 6H), 1.16 (br, m, 6H), 1.55 (br, m, 3H), 6.73 (m, 12H), 8.13 (m, 12H). ^{31}P{^{1}H} NMR (121.5 MHz, C$_6$D$_6$) δ/ppm: 15.2 (d, $^1J_{Rh-P}$ = 83 Hz). UV−vis (THF): λ/nm (ε/M^{-1} cm^{-1}) 268 (14 300), 276 (14 200), 298 (14 200), 342 (14 000), 419 (960). IR (Nujol): $\tilde{\nu}_{C\equiv N}$ = 2223 cm^{-1}. Anal. Calcd for $C_{47}Cl_3F_6H_{39}NP_2Rh$: C, 56.28; H, 3.92; N, 1.40. Found: C, 55.97; H, 3.95; N, 1.40.

Complex 3b. 98% yield; ^{1}H NMR (500 MHz, C$_6$D$_6$) δ/ppm: 1.09 (br, d, 6H), 1.23 (br, m, 6H), 1.62 (br, m, 3H), 7.03 (m, 12H), 8.04

(m, 12H). ^{31}P{^{1}H} NMR (121.5 MHz, C$_6$D$_6$) δ/ppm: 15.0 (d, $^1J_{Rh-P}$ = 84 Hz). UV−vis (THF): λ/nm (ε/M^{-1} cm^{-1}) 274 (sh) (16 900), 282 (15 500), 304 (16 200), 345 (19 500), 422 (950). IR (Nujol): $\tilde{\nu}_{C\equiv N}$ = 2220 cm^{-1}. Anal. Calcd for $C_{47}Cl_9H_{39}NP_2Rh$: C, 51.24; H, 3.57; N: 1.27. Found: C, 51.26; H, 3.46; N, 1.25.

Complex 3c. The reaction mixture was stirred for 6 d. 87% yield; ^{1}H NMR (500 MHz, C$_6$D$_6$) δ/ppm: 1.17 (br, m, 12H), 1.55 (br, m, 3H), 1.94 (s, 18H), 6.95 (m, 12H), 8.40 (m, 12H). ^{31}P{^{1}H} NMR (121.5 MHz, C$_6$D$_6$) δ/ppm: 15.1 (d, $^1J_{Rh-P}$ = 80 Hz). UV−vis (THF): λ/nm (ε/M^{-1} cm^{-1}) 272 (sh) (12 300), 280 (11 600), 315 (14 500), 350 (16 100), 430 (904). IR (Nujol): $\tilde{\nu}_{C\equiv N}$ = 2214 cm^{-1}. Anal. Calcd for $C_{53}Cl_3H_{57}NP_2Rh$: C, 65.01; H, 5.87; N, 1.43. Found: C, 64.87; H, 5.78; N, 1.43. Crystals suitable for single-crystal diffraction analysis were obtained from a benzene solution of **3c** layered with pentane.

Complex 3d. The reaction mixture was stirred for 13 d. 99% yield; ^{1}H NMR (500 MHz, C$_6$D$_6$) δ/ppm: 1.21 (br, m, 6H), 1.27 (br, d, 6H), 1.60 (br, m, 3H), 3.17 (s, 18H), 6.73 (m, 12H), 8.42 (m, 12H). ^{31}P{^{1}H} NMR (121.5 MHz, C$_6$D$_6$) δ/ppm: 13.5 (d, $^1J_{Rh-P}$ = 80 Hz). UV−vis (THF): λ/nm (ε/M^{-1} cm^{-1}) 275 (sh) (22 400), 284 (19 200), 327 (15 100), 359 (15 800), 431 (1090). IR (Nujol): $\tilde{\nu}_{C\equiv N}$ = 2204 cm^{-1}. Anal. Calcd for $C_{53}Cl_3H_{57}NO_6P_2Rh$: C, 59.20; H, 5.34; N, 1.30. Found: C, 59.15; H, 5.28; N, 1.25.

Addition of O$_2$ to 1 To Generate trans-Rh^{III}Cl(CNAd)(η^2-O$_2$)(P(4-X-C$_6$H$_4$)$_3$)$_2$ (4) (X = F (4a), Cl (4b), Me (4c), OMe (4d)). A J. Young NMR tube was charged with a yellow solution of **1a** (20.0 mg, 0.0215 mmol) in 0.7 mL of THF-d_8 at 20 °C. The tube was then flushed with O$_2$ for several minutes in order to achieve 1.0 atm of O$_2$. After the tube was shaken vigorously, the yellow solution rapidly became olive-green. A ^{31}P{^{1}H} NMR spectrum obtained immediately after the addition of O$_2$ showed the quantitative generation of a single product. Spectral data for **4a**: ^{1}H NMR (500 MHz, THF-d_8) δ/ppm: 1.40 (br, d, 6H), 1.51 (br, m, 6H), 1.89 (br, m, 3H), 7.14 (m, 12H), 7.66 (m, 12H). ^{31}P{^{1}H} NMR (121.5 MHz, C$_6$D$_6$) δ/ppm: 27.3 (d, $^1J_{Rh-P}$ = 95 Hz). UV−vis (THF): λ/nm (ε/M^{-1} cm^{-1}) 269 (21 400), 275 (22 000), 290 (sh) (22 300), 304 (24 800). IR (Nujol): $\tilde{\nu}_{O-O}$ = 892 cm^{-1}.

Complex 4b: ^{1}H NMR (500 MHz, THF-d_8) δ/ppm: 1.38 (br, d, 6H), 1.54 (br, m, 6H), 1.90 (br, m, 3H), 7.42 (m, 12H), 7.60 (m, 12H). ^{31}P{^{1}H} NMR (121.5 MHz, C$_6$D$_6$) δ/ppm: 28.5 (d, $^1J_{Rh-P}$ = 95 Hz). UV−vis (THF): λ/nm (ε/M^{-1} cm^{-1}) 273 (33 200), 281 (31 700), 311 (35 900). IR (Nujol): $\tilde{\nu}_{O-O}$ = 890 cm^{-1}. Crystals suitable for single-crystal diffraction analysis were obtained from an oxygenated CH_2Cl_2 solution of **4b** layered with oxygenated pentane.

Complex 4c: ^{1}H NMR (500 MHz, THF-d_8) δ/ppm: 1.29 (br, d, 6H), 1.47 (br, m, 6H), 1.82 (br, m, 3H), 2.32 (s, 18H), 7.12 (m, 12H), 7.53 (m, 12H). ^{31}P{^{1}H} NMR (121.5 MHz, C$_6$D$_6$) δ/ppm: 27.2 (d, $^1J_{Rh-P}$ = 94 Hz). UV−vis (THF): λ/nm (ε/M^{-1} cm^{-1}) 273 (19 000), 281 (19 500), 293 (sh) (20 400), 313 (23 600). IR (Nujol): $\tilde{\nu}_{O-O}$ = 886 cm^{-1}.

Complex 4d: ^{1}H NMR (500 MHz, THF-d_8) δ/ppm: 1.34 (br, d, 6H), 1.47 (br, m, 6H), 1.83 (br, m, 3H), 2.32 (s, 18H), 6.86 (m, 12H), 7.57 (m, 12H). ^{31}P{^{1}H} NMR (121.5 MHz, C$_6$D$_6$) δ/ppm: 24.1 (d, $^1J_{Rh-P}$ = 92 Hz). UV−vis (THF): λ/nm (ε/M^{-1} cm^{-1}) 276 (sh) (32 600), 285 (26 700) (sh), 321 (26 300). IR (Nujol): $\tilde{\nu}_{O-O}$ = 888 cm^{-1}.

X-ray Crystallographic Details. All structures were collected on a Bruker three-circle platform goniometer equipped with an Apex II CCD and an Oxford cryostream cooling device at 100 K. Radiation was generated from a graphite fine focus sealed tube Mo Kα (0.71073 Å) source. Crystals were mounted on a cryoloop using Paratone N oil. Data were integrated using SAINT and scaled with a multiscan absorption correction using SADABS. The structures were solved by direct methods or Patterson methods using SHELXS-97 and refined against F^2 on all data by full matrix least-squares with SHELXL-97. All non-hydrogen atoms were refined anisotropically. Hydrogen atoms bound to carbon were placed at idealized positions and refined using a riding model. For hydride complex **2**, the rhodium-bound hydrogen atom was tentatively located in the difference map and refined isotropically. For **2a**, the adamantyl group was modeled as a two-part positional disorder, and rigid bond restraints were used on all
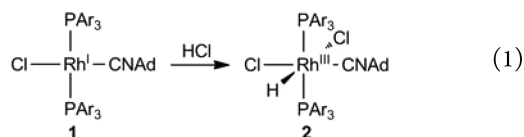
Table 1. Crystal Data and Structure Refinement

	2a	2c · 2 CH$_2$Cl$_2$	2d · 2 CH$_2$Cl$_2$	3c	4b
formula	C$_{47}$H$_{40}$Cl$_2$F$_6$NP$_2$Rh	C$_{55}$H$_{62}$Cl$_6$NP$_2$Rh	C$_{55}$H$_{62}$Cl$_6$NO$_6$P$_2$Rh	C$_{53}$H$_{57}$Cl$_3$NP$_2$Rh	C$_{47}$H$_{39}$Cl$_7$NO$_2$P$_2$Rh
fw, g/mol	968.55	1114.61	1210.65	979.20	1062.79
temperature, K	100(2)	100(2)	100(2)	100(2)	100(2)
cryst syst	orthorhombic	orthorhombic	triclinic	monoclinic	triclinic
space group	Pnma	Pbca	P−1	P2$_1$/n	P−1
color	colorless	colorless	colorless	yellow	yellow
a/Å	16.990(3)	16.5395(7)	13.3051(9)	18.263(2)	12.9496(19)
b/Å	24.487(5)	19.8373(8)	13.6577(9)	11.8140(14)	13.1190(19)
c/Å	9.888(2)	32.8349(13)	14.9952(10)	22.133(3)	15.028(2)
α/deg	90	90	91.2690(10)	90	109.318(2)
β/deg	90	90	94.8890(10)	106.735(2)	105.716(2)
γ/deg	90	90	106.6240(10)	90	97.509(2)
V/Å^3	4113.7(14)	10773.1(8)	2598.4(3)	4573.2(10)	2263.7(6)
Z	4	8	2	4	2
R$_1$^{a}	0.035	0.039	0.030	0.048	0.087
wR$_2$^{b}	0.084	0.11	0.073	0.11	0.18
GOF (F^2)^c	1.02	1.05	1.06	1.04	1.07

^{a}R1 = $\Sigma\|F_0 - F_c\|/\Sigma|F_0|$. ^{b}wR2 = $(\Sigma(w(F_0^2 - F_c^2)^2)/\Sigma(w(F_0^2)^2))^{1/2}$. ^{c}GOF = $(\Sigma w(F_0^2 - F_c^2)^2/(n - p))^{1/2}$ where n is the number of data, and p is the number of parameters refined.

disordered atoms. For all structures, the corresponding 1−2 and 1−3 distances of the adamantly group were restrained to be identical. The crystal structure of **2b** was heavily disordered and could not be satisfactorily refined. The crystal structure of **2d** contained multiple disordered CH$_2$Cl$_2$ molecules that could not be modeled satisfactorily. Therefore, electron density associated with the disordered solvent was removed using the SQUEEZE program. The crystals of **3c** and **4b** were each twinned over two domains, which were identified using the program CELL_NOW. The program TWINABS was used for absorption correction. Crystal data and refinement statistics are summarized in Table 1.

■ RESULTS

Reaction of 1 with HCl and O$_2$. Complex **1** reacts with HCl to generate the corresponding hydride complex, *cis,trans*-
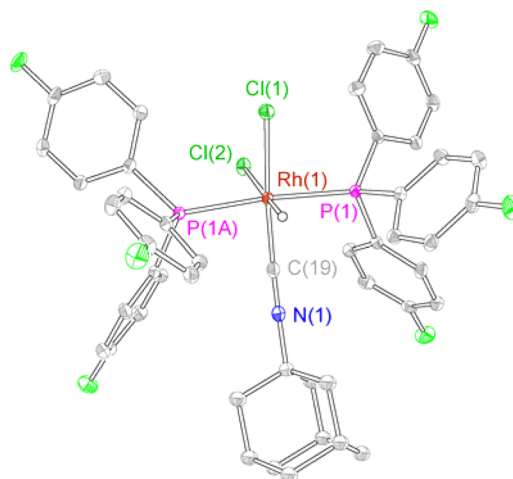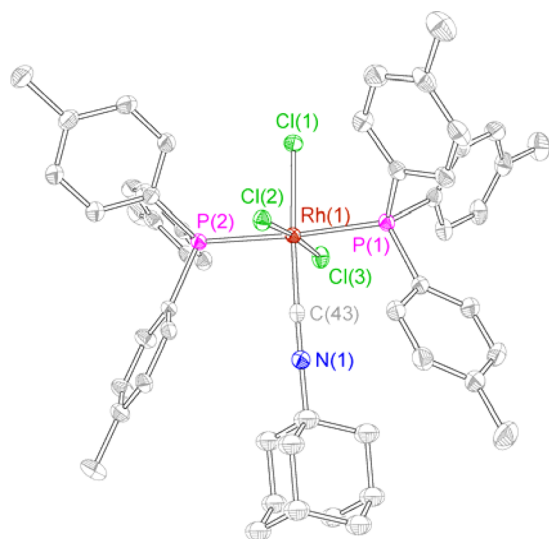

Figure 1. Thermal ellipsoid plot of **2a** shown at the 50% probability level. Carbon-bound hydrogen atoms are omitted for clarity. Data were collected at 100(2) K.

$$Cl\!-\!\underset{\underset{PAr_3}{|}}{\overset{\overset{PAr_3}{|}}{Rh^I}}\!-\!CNAd \xrightarrow{HCl} Cl\!-\!\underset{\underset{PAr_3}{|}}{\overset{\overset{PAr_3}{|}}{\underset{H}{Rh^{III}}}}\!\overset{Cl}{\underset{}{}}\!-\!CNAd \qquad (1)$$

1 → **2**

Rh^{III}Cl$_2$H(CNAd)(P(4-X-C$_6$H$_4$)$_3$)$_2$ (**2**) By means of ^{1}H and ^{31}P{^{1}H} NMR spectroscopy, the hydride complex is shown to form rapidly and quantitatively upon treatment of **1** with excess HCl. Additionally, **2** can be isolated as a colorless solid and stored indefinitely under an inert atmosphere. In some cases, the formation of a small amount of yellow solid was observed that we ascribe to the reversion of hydride complex **2** to the starting complex **1** upon removal of solvent *in vacuo*. In this case, **2** was resuspended in pentane, and a small amount of excess HCl was added to the suspension. The solvent was removed to give **2** as a pure, colorless solid. Purity was confirmed by NMR and elemental analysis.

The stereochemistry of **2** was determined by means of single crystal X-ray diffraction, and the thermal ellipsoid plot of **2a** is provided in Figure 1 as a representative example of the structure of the hydride complexes. For each of the four hydride complexes **2a−d**, ^{1}H NMR, ^{31}P{^{1}H} NMR, and X-ray crystallography data indicate that the Rh^{III} metal center exhibits an octahedral coordination geometry in which the two PAr$_3$

ligands are arranged in a trans geometry whereas the two Cl ligands are arranged in a cis geometry. Notably, the trans influence of the hydride ligand results in a distinctly longer bond distance for the Cl ligand that is trans to the hydride compared to the Cl ligand that is cis to the hydride. Using **2a** as an example, the Rh(1)−Cl(2) bond distance (2.4954(1) Å) is longer than that of Rh(1)−Cl(1) (2.4073(2) Å).

The addition of O$_2$ to CH$_2$Cl$_2$ or THF solutions of **2** containing excess HCl results in the immediate consumption of **2** and generation of *trans*-Rh^{III}Cl$_3$(CNAd)(P(4-X-C$_6$H$_4$)$_3$)$_2$ (**3**), an aqua complex, *cis,trans*-[Rh^{III}(OH$_2$)Cl$_2$(CNAd)(P(4-X-C$_6$H$_4$)$_3$)$_2$]Cl (**5**), and water, as shown by ^{31}P{^{1}H} and ^{1}H NMR spectral data.

The ratio of the *trans*-Rh^{III}Cl$_3$ species (**3**) to aqua complex (**5**) is variable and appears to be highly sensitive to the reaction conditions. In some cases, the ratio of the *trans*-Rh^{III}Cl$_3$ complex to the aqua complex can be as high as 4:1, whereas in other cases, the ratio can be as low as 1:1. In all cases, over the course of several days, the ^{31}P{^{1}H} and ^{1}H NMR spectral

features corresponding to the aqua complex disappear as the shifts corresponding to the *trans*-Rh^{III}Cl$_3$ complexes (**3**) and unbound water intensify. This observation is consistent with the assignment of **5** as an aqua complex. It should also be noted that the amount of water present does not affect the rate of conversion of **5** to **3** (*vide infra*). In the case of **2c/d**, the ORR yields a small amount (ca. 10%) of a third product with ^{31}P{^{1}H} and ^{1}H NMR spectral features consistent with a complex of the form *fac*-Rh^{III}Cl$_3$(CNAd)(P(4-X-C$_6$H$_4$)$_3$)$_2$ (**6c/d**). The spectral features of **6c/d** are also observed upon the addition of PhICl$_2$ to **1c/d** in the synthesis of **3c/d**. After several days of stirring, the ^{31}P{^{1}H} NMR spectrum of the reaction mixture shows that **3c/d** is the only phosphorus-containing species in solution, thus indicating that **6c/d** thermally isomerizes to render **3c/d**. Running the ORR of **2** with O$_2$ in THF in the presence of HCl, and layering that reaction mixture with pentane, furnishes large yellow crystals of **3**. X-ray quality crystals of **5** or **6** could not be obtained. A thermal ellipsoid plot of **3c** is provided in Figure 2 as a representative example of the structure of the *trans*-Rh^{III}Cl$_3$ species **3**.

Figure 2. Thermal ellipsoid plot of **3c** shown at the 50% probability level. Carbon-bound hydrogen atoms are omitted for clarity. Data were collected at 100(2) K.

In order to confirm that the ORR does indeed generate water, the ORR was performed using the deuteride analogue of **2a**, **2a**^{d}, in a THF solution containing excess DCl and O$_2$. Immediately after the reaction was performed, ^{2}H NMR revealed a broad singlet at δ 3.26 ppm and another broad singlet at δ 6.59 ppm, which correspond to free D$_2$O and D$_2$O-bound complexes, respectively, in a roughly 1:1 ratio. Additionally, ^{31}P{^{1}H} NMR shows a doublet at δ 15.2 ppm ($^1J_{Rh-P}$ = 83 Hz), which corresponds to **3a**, and another doublet at δ 15.4 ppm ($^1J_{Rh-P}$ = 81 Hz), which corresponds to the Rh^{III}-aqua complex. Over the course of several days, ^{2}H NMR shows that the shift at δ 3.26 ppm grows as the shift at δ 6.59 ppm diminishes relative to the THF-d_8 peaks. Similarly, ^{31}P{^{1}H} NMR shows that the doublet at δ 15.4 ppm disappears and only the shift at δ 15.2 ppm remains. Although the aqua complex could not be isolated, the above spectral data are consistent with its formation. Additionally, the identification of D$_2$O, whether free or bound, as the sole deuterium-containing

product confirms that the hydride species **2** does indeed effect the reduction of O$_2$ to H$_2$O. The stoichiometry of the ORR is uncertain because the fate of the second oxygen atom of O$_2$ is not yet known. One possible fate of the second oxygen atom is that protonation of a putative hydroperoxo complex releases water and generates an unstable high-valent oxo species which rapidly decomposes, presumably by reaction with solvent. Such reactivity has been characterized for other synthetic metal-hydroperoxo complexes, where a high-valent oxo complex is observed or inferred upon acid-induced O−O bond heterolysis.[36−38] However, the data provided herein does not offer insight into such a decomposition pathway, as only complexes **3**, **5**, and **6** can be observed upon treatment of **4** with HCl (*vide infra*).

Reaction of 1 with O$_2$ To Form *trans*-Rh^{III}Cl(CNAd)(η^2-O$_2$)(P(4-X-C$_6$H$_4$)$_3$)$_2$ (4). Addition of 1 atm of O$_2$ to **1** results in the immediate formation of the corresponding peroxo complex **4**. ^{31}P{^{1}H} and ^{1}H NMR spectra obtained immediately after the
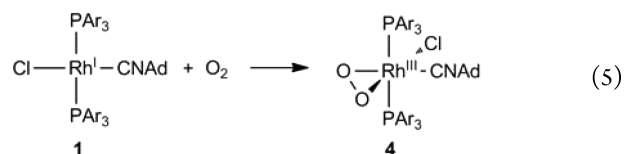
addition of O$_2$ and manual shaking of the sample show resonances corresponding to complex **4**. The ^{31}P{^{1}H} NMR spectrum of the peroxo species **4** shows a single doublet with a rhodium−phosphorus coupling constant ranging from 92 to 95 Hz. X-ray crystal structure and infrared spectroscopy data confirm that the product of this reaction is indeed a *trans*-Rh^{III}Cl(CNAd)(η^2-O$_2$)(P(4−X−C$_6$H$_4$)$_3$)$_2$ complex. The crystallographic data and spectral features of **4** are consistent with those of related Rh^{III}(η^2-O$_2$) complexes.[5,34,39,40]

The X-ray crystal structure of **4b**, which is provided in Figure 3, reveals that O$_2$ binds to the Rh^{III} metal center as an η^2-peroxo. The O(1)−O(2) bond distance is 1.417(7) Å, which indicates that O$_2$ binds as an O$_2$$^{2−}$ ligand with an O−O single bond.[40−42] Taking the midpoint of the O−O vector to occupy a coordination site, the coordination environment about Rh^{III} is approximately trigonal bipyramidal. Such a coordination
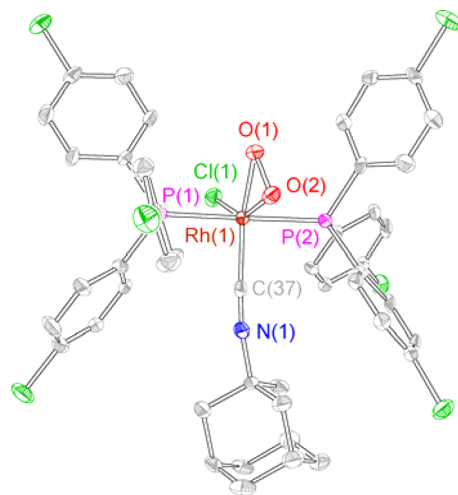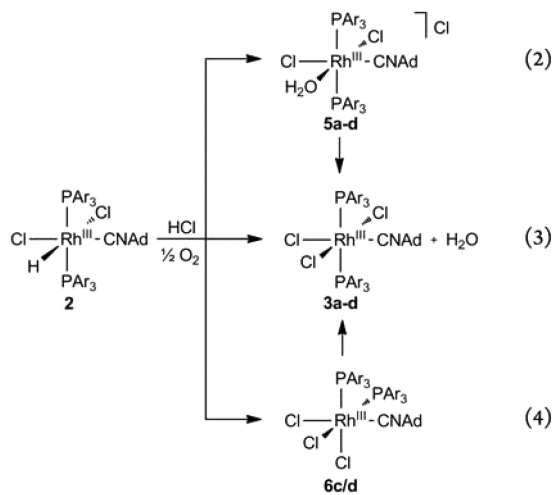

Figure 3. Thermal ellipsoid plot of **4b** shown at the 50% probability level. Hydrogen atoms are omitted for clarity. Data were collected at 100(2) K.

geometry is consistent with $^{31}P\{^1H\}$ and ^1H NMR data for each peroxo complex, which indicate that the two phosphine ligands are trans to one another. Although **4a**, **4c**, and **4d** were not structurally characterized, the observation that **4a−d** all possess similar spectral features is consistent with structural homology between the four peroxo complexes.

$^{31}P\{^1H\}$ and ^1H NMR data indicate that peroxo complex **4** is stable in solution at ambient temperatures under 1 atm of O_2 for several hours but decomposes to O=PAr$_3$ and a mixture of intractable rhodium-containing products overnight. Hence, although saturated solutions of **4** could be cooled or layered to afford crystalline samples, unidentified contaminants were always present. Additionally, O_2 addition to **1** is reversible. By means of several freeze−pump−thaw cycles on a high-vacuum manifold, solutions samples of **4** can be gradually reverted to **1** without decomposition. In a similar vein, solutions of **4** brought to dryness *in vacuo* furnish a mixture of **4** and **1**.

The addition of 5 mol equiv of HCl to an oxygenated THF solution of the peroxo species **4** immediately results in the formation of a mixture of the *trans*-Rh^{III}Cl$_3$ and Rh^{III}-aqua complexes, **3** and **5**, respectively, in variable proportions. In the case of **4c/d**, a small amount of *fac*-Rh^{III}Cl$_3$ **6** also forms. Thus, treatment of **4** with excess HCl results in immediate O−O bond cleavage to furnish the products of the ORR of **2**, thus establishing the peroxo complex **4** as a plausible intermediate in the ORR of **2**.

Rate Law for the Reaction of 2 with HCl and O₂ To Form 3. The kinetic profile for the reaction of each rhodium hydride complex **2** with HCl and O_2 was determined. The reaction proceeds as shown in eqs 2−4. The UV−vis

absorption bands of the hydride complex **2** are obscured by those of **3**, **5**, and **6** (if present), which grow in during the course of the ORR. Thus, the rate of disappearance of **2** could not be measured by monitoring the disappearance of bands that correspond to **2**. Instead, the progress of the reaction was tracked by monitoring the growth of an absorbance (λ_{max}), which is not obscured by the absorbance bands of **2**, that corresponds to the linear combination of absorbances of the products of **3**, **5**, and **6** (if present)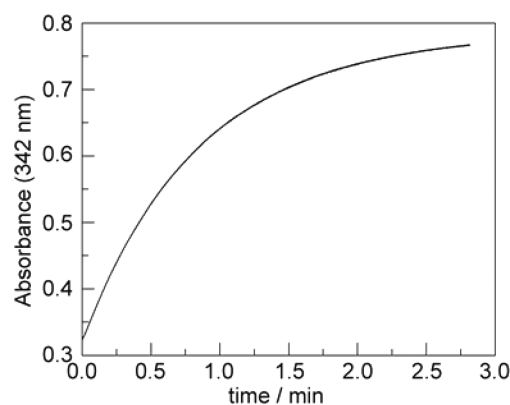. A representative kinetic trace for the reaction of **2a** with O_2 (0.80 atm) and HCl (30 mM), showing the change in the absorbance at 342 nm (A$_{342 nm}$) versus time, is provided in Figure 4.

The kinetic trace of the growth of λ_{max} exhibits a well-defined monoexponential fit under pseudo-first-order conditions. Using

Figure 4. Representative kinetic trace for the reaction of **2a** with O_2 (0.80 atm) and HCl (30 mM), showing the change in the absorbance at 342 nm (A$_{342 nm}$) vs time.

UV−vis absorbance spectroscopy to measure k_{obs} and $^{31}P\{^1H\}$ NMR to measure the molar distribution of products, it was found that k_{obs} is invariant to the molar ratios of **3**, **5**, and **6** (if present) formed by the ORR. This indicates that the processes that affect the molar distribution of products occur after the rate-determining step and thus have no kinetic impact. Accordingly, monitoring the rate of growth of λ_{max}, which is the linear sum of the absorbances of **3**, **5**, and **6** (if present), corresponds to measuring the rate of disappearance of **2** and provides a rate law of the ORR. This is supported by the fact that measuring the growth of absorption bands at various other wavelengths does not significantly change the value of k_{obs}. The λ_{max} absorbances measured for **3a**, **3b**, **3c**, and **3d** were 342, 345, 350, and 359 nm, respectively. It should also be noted that the time scale of each kinetic trace for the conversion of **2** to **3** is on the order of minutes, whereas the conversions of **5** and **6** to **3** takes several days, and thus, these latter conversions have no impact on this kinetics study of **2** converting to **3**.

The value of k_{obs} depends on both the O_2 partial pressure, p(O_2), and the HCl concentration. Figure 5 shows the dependence of k_{obs} on the partial pressure of O_2 at four different HCl concentrations for each hydride complex **2**. At constant [HCl], k_{obs} varies linearly with p(O_2), and the y-intercept for each best-fit line is effectively zero. This indicates that each term of the rate law exhibits a first-order dependence on p(O_2). Figure 6 shows that the slopes of the plots in Figure 5 vary linearly with [HCl]$^{-1}$ to give a nonzero y-intercept, which suggests a two-term rate law in which one term is inverse-first-order in HCl and the other term is zero-order in HCl. Combined, Figures 5 and 6 indicate that the reaction of **2** with HCl and O_2 obeys the following two-term rate law:

$$\text{rate} = \frac{k_1[\mathbf{2}][O_2]}{[\text{HCl}]} + k_1'[\mathbf{2}][O_2] = \{k_1^{\text{HCl}} + k_1'\}[\mathbf{2}][O_2]$$

(6)

where $k_1^{\text{HCl}} = k_1/[\text{HCl}]$. The reaction of **2** with HCl and O_2 thus gives rise to two first-order rate constants, k_1 and k_1'. The values of these rate constants are obtained from the best-fit lines in Figure 6 and are provided in Table 2. The values of k_1 and k_1' are obtained from the slopes and y-intercepts of Figure 6, respectively.

Additionally, running the reaction of **2** with HCl and O_2 in the presence of BHT (1.1 mM) does not diminish the values of k_{obs}. For example, in the absence of BHT, the reaction of **2a** with 1.4 atm of O_2 and 59 mM of HCl gives $k_{obs} = 1.09$ min^{-1}.
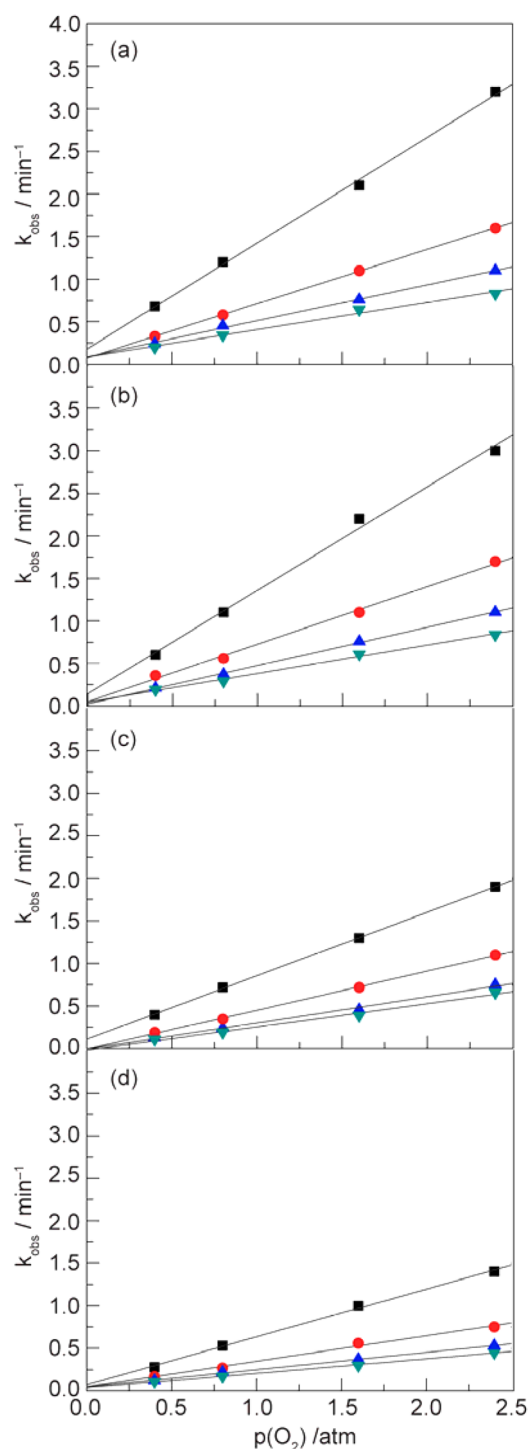
Figure 5. Dependence of k_{obs} on $p(O_2)$ for the reaction of (a) **2a**, (b) **2b**, (c) **2c**, and (d) **2d** with O_2 and HCl, with [HCl] at 30 mM (black ■), 59 mM (red ●), 91 mM (blue ▲), and 120 mM (green ▼). Each data point is the statistical average of three measurements; the error bars are within the size of the symbols. The solid lines show the best-fit lines for each data set.

Figure 6. Slopes of the best-fit lines of k_{obs} vs $p(O_2)$ from Figure 5a (black ●), b (brown ■), c (orange ▼), and d (green ▲) are plotted against $[HCl]^{-1}$. The best-fit line is shown.

Table 2. Rate Constants As Defined by Eq 6, for the Reaction of 2 with HCl and O_2

X	k_1/min^{-1} atm^{-1} M^a	k_1^{HCl}/min^{-1} atm$^{-1a,b}$	$k_1{'}$/min^{-1} atm^{-1a}
F	0.0355 ± 0.0003	1.17 ± 0.01	0.029 ± 0.006
Cl	0.035 ± 0.001	1.16 ± 0.03	0.070= ± 0.02
Me	0.0194 ± 0.0009	0.64 ± 0.03	0.11 ± 0.02
OMe	0.0160 ± 0.0004	0.53 ± 0.01	0.030 ± 0.007

^{a}Rate constants defined in eq 6. ^{b}This term was measured for four HCl concentrations of 8.3, 11, 17, and 33 M^{-1}. The data shown here are for $[HCl]^{-1}$ = 33 M^{-1}. A complete listing of k_1^{HCl} for all four concentrations is provided in Table S1.

radical-chain autoxidation pathway. Additionally, the k_{obs} is not significantly altered if the reaction is run in the presence of additional water, although the distribution of **3**, **5**, and **6**, does change, as shown by $^{31}P\{^1H\}$ and ^1H NMR.
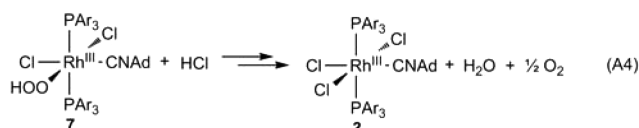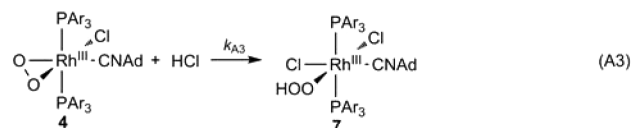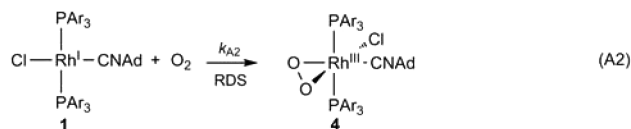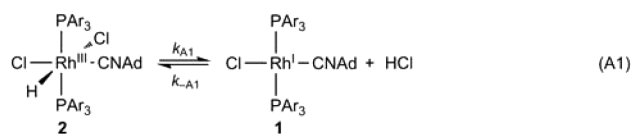
■ DISCUSSION

Mechanism of O_2 Reduction by 2. The kinetic studies described herein furnish the two-term rate law given in eq 6. The two-term rate law indicates that the reaction of **2** with HCl and O_2 proceeds along two parallel reaction pathways. The steps of these pathways are provided in Scheme 1 and agree well with the kinetic data. Accordingly, eq 6 can be rewritten as

$$\frac{d[\mathbf{3}]}{dt} = \frac{k_{A1}k_{A2}[\mathbf{2}][O_2]}{k_{-A1}[HCl]} + k_{B1}[\mathbf{2}][O_2] \tag{7}$$
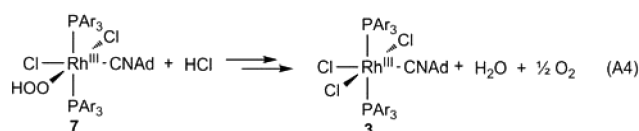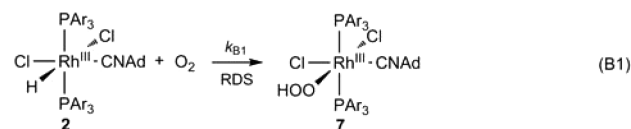
where $k_1 = k_{A1}k_{A2}/k_{-A1} = K_{A1}k_{A2}$ and $k_1{'} = k_{B1}$. The first term of the rate law is inverse-first-order in HCl and first-order in O_2, which is consistent with the HXRE pathway. The inverse HCl dependence indicates that HCl reductive elimination precedes the rate-determining step, and the first-order O_2 dependence indicates that the reaction with O_2 is rate-limiting. The proposed HXRE term differs from that reported by Stahl and Konnick, whose mechanistic studies on insertion of O_2 into a Pd(II)-hydride bond revealed a zero-order dependence on O_2 for the HXRE mechanism and that the rate-determining step was HX reductive elimination.[28] Our results are consistent with the formation of the peroxo complex **4**, although such an intermediate species is not spectroscopically observed during the course of the reaction. Subsequent elementary steps occur beyond the rate-determining step and thus have no kinetic impact; however, based on the reactivity of the related diiridium

However, running the same reaction in the presence of 1.1 mM of BHT gives the pseudo-first-order rate constant of 1.30 min^{-1}. Similarly, the reaction of **2c** with 1.4 atm of O_2 and 59 mM of HCl in the absence of BHT gives k_{obs} = 0.715 min^{-1}, whereas the reaction in the presence of BHT gives k_{obs} = 0.819 min^{-1}. These results indicate that the ORR does not involve a

Scheme 1

HXRE Pathway

(A1)

(A2)

(A3)

(A4)

HAA Pathway

(B1)

(A4)

system, $Ir_2^{II,II}(tfepma)_2(CN^tBu)_2Cl_2(\eta^2\text{-}O_2)$, protonation of **4** to generate the putative hydroperoxo species **7** appears likely.[25] The second term of the rate law is only first-order in O_2, which is consistent with the HAA pathway. In this pathway, the hydride complex **2** reacts directly with O_2 to generate a hydroperoxide intermediate **7**. Support for the formation of **7** comes from computational and kinetic studies which indicate that the formation of a hydroperoxide complex via hydrogen-atom abstraction is a viable mechanistic pathway for Pd^{II} complexes.[16,17,28−33] Additionally, further computational and experimental studies have demonstrated that the HXRE and HAA pathways are close in energy and capable of operating competitively,[25,30,33,34] as is the case for this study.

For both the HXRE and HAA pathways, the reaction of the putative hydroperoxo species **7** to give **3** with concomitant formation of water occurs after the rate-determining step and therefore has no kinetic impact on the ORR. As a result, the nature of the reactivity of **7** is unclear. It is possible that **7** evolves a hydroxide complex, as has been proposed and observed for other hydroperoxides of platinum group metals,[17,18,43,44] and subsequently undergoes protonolysis to release water. Further studies will be required in order to provide insight into the reactivity of **7**.

Analysis of the Effects of Electronic Variation upon the HXRE and HAA Pathways. Given the competition between the HXRE and HAA pathways, a series of electronically varied hydride complexes **2** were prepared in order to

elucidate what factors, particularly with regard to ligand environment, govern the kinetics and preferred mechanistic pathways of aerobic oxidation reactions for metal hydride complexes. The reactivity of **2** was modulated by varying the substituents in the para position of the PAr_3 ligands, and spectroscopic and kinetic studies confirm that the electronic structure of **2** systematically varies as a function of the electronic properties of the para substituent. For example, the ^1H NMR shift of the hydride ligand for **2** varies linearly as a function the Hammett parameter, σ_p, for the substituents, as shown in Figure 7.
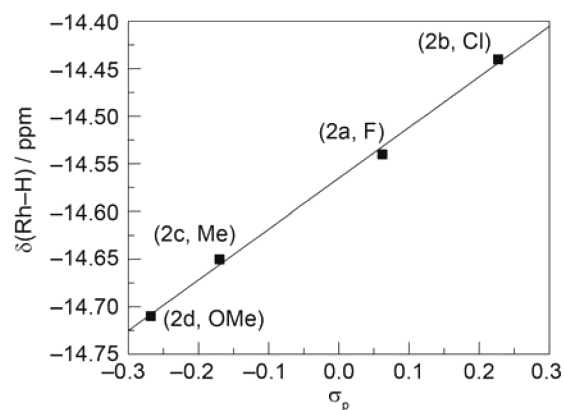

Figure 7. Dependence of $\delta(Rh-H)$ (CD_2Cl_2, 20 °C) on σ_p.

The rate constant of the HXRE pathway, k_1, increases with increasingly electron-withdrawing substituents. This observation can be rationalized in that increasingly electron-withdrawing substituents will in turn lead to increasingly oxidized metal centers, which are more prone toward reductive elimination of HX via the HXRE pathway.[33,40−42] In other words, K_{A1} is augmented as increasingly electron-poor phosphines are incorporated. Accordingly, a plot of log k_1 for the hydride complexes **2** reveals an approximately linear correlation with the σ_p Hammett parameter for each substituent, as shown in Figure 8a. In the case of the HAA term, the rate constant k_1' does not linearly correlate with the Hammett parameters. However, a plot of log k_1' versus the Rh−H stretching frequency, $\tilde{\nu}(Rh-H)$, shows that the rate of the HAA pathway varies linearly as a function of the Rh−H stretching frequency, as shown in in Figure 8b. This trend in the HAA pathway can be rationalized by noting that a smaller value of $\tilde{\nu}(Rh-H)$ corresponds to a smaller Rh−H bond dissociation energy which in turn leads to a greater HAA rate constant, k_1'. In this way, k_1' mirrors the strength of the Rh−H bond.

These results show that not only can the insertion of O_2 into a Rh^{III}−H bond occur by different mechanisms, but that the preferred pathway can be influenced by tuning the electron-donating or withdrawing properties of the ancillary ligand set. The observed linear trend between the HXRE rate constant and the Hammett parameter is expected due to the fact that the HXRE step is an acid−base reaction and thus follows the polar effects that the Hammett parameter empirically quantifies. On the other hand, the HAA pathway is a radical pathway and its rate is governed by the strength of the Rh−H bond. Accordingly, the observation that the HAA rate constant does not correlate linearly with the Hammett parameter is unsurprising and does not indicate that the HAA pathway is
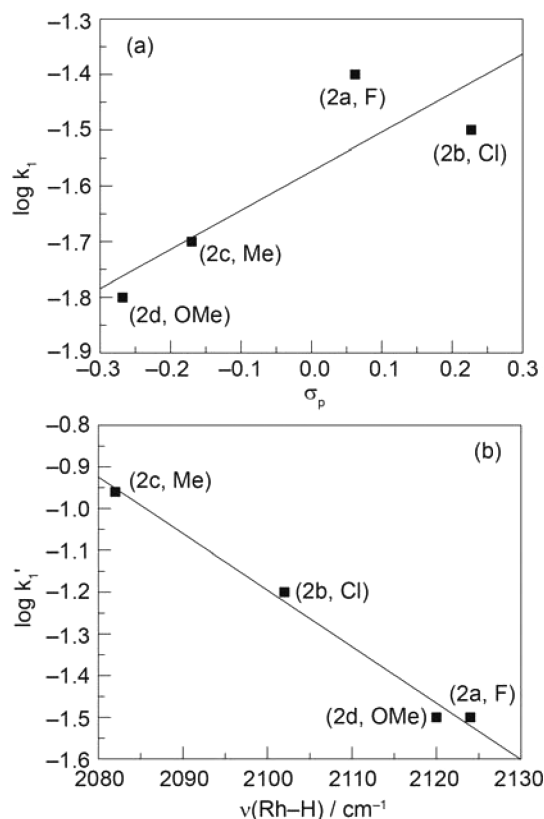
Figure 8. Dependence of (a) log k_1 on σ_p and (b) log k_1' on ν(Rh−H) for **2**.

immune to systematic tuning by means of varying the electronic properties of the ancillary ligand set. Rather, a systematic trend between the rate of the HAA pathway and the electronic properties of **2** is evidenced by the linear correlation between log k_1' and $\tilde{\nu}$(Rh−H), which reflects the Rh−H bond order. Thus, tuning the electronic properties of the ancillary ligand set does lead to systematic variation in the rates of the HXRE and HAA pathways, but the rates of the two pathways vary independently of each other. It is worth noting that the HXRE and HAA pathways become more competitive with increasing concentration of HCl, especially in the case of **2c**. However, the HXRE pathway is predominate over the surveyed range of acid concentrations.

In conclusion, the studies herein provide insight into the factors which govern the reduction of O_2 to H_2O by a series of electronically varied rhodium(III) hydride complexes. Synthetic and kinetic studies reveal that the hydride complex **2** reacts with HCl and O_2 to effect the reduction of O_2 to water according to a two-term rate law, which comprises parallel and competitive HXRE and HAA pathways. It was observed that the rate of the HXRE pathway was promoted by increasingly electron-withdrawing PAr_3 ligands, which result in increasingly electron-deficient metal centers. In addition, the rate of the HAA pathway is promoted as the Rh−H bond strength is weakened.

■ ASSOCIATED CONTENT

ⓢ Supporting Information

Electronic absorption spectra for complexes **1a−d**, **2a−d**, **3a−d**, and **4a−d**, and crystallographic information file (CIF). The

Supporting Information is available free of charge on the ACS Publications website at DOI: 10.1021/acs.inorgchem.5b00856.

■ AUTHOR INFORMATION

Corresponding Author
*E-mail: dnocera@fas.harvard.edu.

Notes
The authors declare no competing financial interest.

■ ACKNOWLEDGMENTS

■ REFERENCES

(1) Stahl, S. S. *Angew. Chem., Int. Ed.* **2004**, *43*, 3400−3420.
(2) Punniyamurthy, T.; Velusamy, S.; Iqbal, J. *Chem. Rev.* **2005**, *105*, 2329−2363.
(3) Lippert, C. A.; Arnstein, S. A.; Sherrill, C. D.; Soper, J. D. *J. Am. Chem. Soc.* **2010**, *132*, 3879−3892.
(4) Klinman, J. P. *Chem. Rev.* **1996**, *96*, 2541−2561.
(5) Meier, G.; Braun, T. *Angew. Chem., Int. Ed.* **2011**, *50*, 3280−3284.
(6) Stahl, S. S. *Science* **2005**, *309*, 1824−1826.
(7) Kunisu, T.; Oguma, T.; Katsuki, T. *J. Am. Chem. Soc.* **2011**, *133*, 12937−12939.
(8) Frazier, C. P.; Engelking, J. R.; de Alaniz, J. R. *J. Am. Chem. Soc.* **2011**, *133*, 10430−10433.
(9) Liu, L.; Yu, M.; Wayland, B. B.; Fu, X. *Chem. Commun.* **2010**, *46*, 6353−6355.
(10) Li, H.; Wei, W.; Xu, Y.; Zhang, C.; Wan, X. *Chem. Commun.* **2011**, *47*, 1497−1499.
(11) Fries, P.; Halter, D.; Kleinschek, A.; Hartung, J. *J. Am. Chem. Soc.* **2011**, *133*, 3906−3912.
(12) Jiang, B.; Feng, Y.; Ison, E. A. *J. Am. Chem. Soc.* **2008**, *130*, 14462−14464.
(13) Chuang, G. J.; Wang, W.; Lee, E.; Ritter, T. *J. Am. Chem. Soc.* **2011**, *133*, 1760−1762.
(14) Thyagarajan, S.; Incarvito, C. D.; Rheingold, A. L.; Theopold, K. H. *Chem. Commun.* **2001**, 2198−2199.
(15) Atlay, M. T.; Preece, M.; Strukul, G.; James, B. R. *J. Chem. Soc., Chem. Commun.* **1982**, 406−407.
(16) Konnick, M. M.; Gandhi, B. A.; Guzei, I. A.; Stahl, S. S. *Angew. Chem., Int. Ed.* **2006**, *45*, 2904−2907.
(17) Denney, M. C.; Smythe, N. A.; Cetto, K. L.; Kemp, R. A.; Goldberg, K. I. *J. Am. Chem. Soc.* **2006**, *128*, 2508−2509.
(18) Wick, D. D.; Goldberg, K. I. *J. Am. Chem. Soc.* **1999**, *121*, 11900−11901.
(19) Look, J. L.; Wick, D. D.; Mayer, J. M.; Goldberg, K. I. *Inorg. Chem.* **2009**, *48*, 1356−1369.
(20) Roberts, H. L.; Symes, W. R. *J. Chem. Soc. A* **1968**, 1450−1453.
(21) Gillard, R. D.; Heaton, B. T.; Vaughan, D. H. *J. Chem. Soc. A* **1970**, 3126−3130.
(22) Cui, W.; Wayland, B. B. *J. Am. Chem. Soc.* **2006**, *128*, 10350−10351.
(23) Szajna-Fuller, E.; Bakac, A. *Inorg. Chem.* **2010**, *49*, 781−785.
(24) Teets, T. S.; Cook, T. R.; McCarthy, B. D.; Nocera, D. G. *J. Am. Chem. Soc.* **2011**, *133*, 8114−8117.
(25) Teets, T. S.; Nocera, D. G. *J. Am. Chem. Soc.* **2011**, *133*, 17796−17806.
(26) Endicott, J. F.; Wong, C.; Inoue, T.; Natarajan, P. *Inorg. Chem.* **1979**, *18*, 450−454.
(27) Stahl, S. S.; Decharin, N. *J. Am. Chem. Soc.* **2011**, *133*, 5732−5735.
(28) Konnick, M. M.; Stahl, S. S. *J. Am. Chem. Soc.* **2008**, *130*, 5753−5762.
(29) Decharin, N.; Popp, B. V.; Stahl, S. S. *J. Am. Chem. Soc.* **2011**, *133*, 13268−13271.

(30) Popp, B. V.; Stahl, S. S. *J. Am. Chem. Soc.* **2007**, *129*, 4410−4422.

(31) Keith, J. M.; Nielsen, R. J.; Oxgaard, J.; Goddard, W. A., III. *J. Am. Chem. Soc.* **2005**, *127*, 13172−13179.

(32) Keith, J. M.; Muller, R. P.; Kemp, R. A.; Goldberg, K. I.; Goddard, W. A., III; Oxgaard, J. *Inorg. Chem.* **2006**, *45*, 9631−9633.

(33) Konnick, M. M.; Decharin, N.; Popp, B. V.; Stahl, S. S. *Chem. Sci.* **2011**, *2*, 326−330.

(34) Keith, J. M.; Teets, T. S.; Nocera, D. G. *Inorg. Chem.* **2012**, *51*, 9499−9507.

(35) Teets, T. S.; Nocera, D. G. *Inorg. Chem.* **2012**, *51*, 7192−7201.

(36) Takahashi, Y.; Hashimoto, M.; Hikichi, S.; Akita, M.; Moro-oka, Y. *Angew. Chem., Int. Ed.* **1999**, *38*, 3074−3077.

(37) Konnick, M. M.; Guzei, I. A.; Stahl, S. S. *J. Am. Chem. Soc.* **2004**, *126*, 10212−10213.

(38) Wang, W.-D.; Bakac, A.; Espenson, J. H. *Inorg. Chem.* **1995**, *34*, 4049−4056.

(39) Meier, G.; Braun, T. *Angew. Chem., Int. Ed.* **2012**, *51*, 12564−12569.

(40) Cipot-Wechsler, J.; Covelli, D.; Praetorius, J. M.; Hearns, N.; Zenkina, O. V.; Keske, E. C.; Wang, R.; Kennepohl, P.; Crudden, C. M. *Organometallics* **2012**, *31*, 7306−7315.

(41) Dickman, M. H.; Pope, M. T. *Chem. Rev.* **1994**, *94*, 569−584.

(42) Cramer, C. J.; Tolman, W. B. *Acc. Chem. Res.* **2007**, *40*, 601−608.

(43) Prokopchuk, E. M.; Jenkins, H. A.; Puddephatt, R. J. *Organometallics* **1999**, *18*, 2861−2866.

(44) Rostovtsev, V. V.; Henling, L. M.; Labinger, J. A.; Bercaw, J. E. *Inorg. Chem.* **2002**, *41*, 3608−3619.

(45) Low, J. J.; Goddard, W. A., III. *J. Am. Chem. Soc.* **1986**, *108*, 6115−6128.

(46) Brown, M. P.; Puddephatt, R. J.; Upton, C. E. E.; Lavington, S. W. *J. Chem. Soc., Dalton Trans.* **1974**, 1613−1618.

(47) Culkin, D. A.; Hartwig, J. F. *J. Am. Chem. Soc.* **2001**, *123*, 5816−5817.